



Open Archive Toulouse Archive Ouverte (OATAO)

OATAO is an open access repository that collects the work of some Toulouse researchers and makes it freely available over the web where possible.

This is an author's version published in: <https://oatao.univ-toulouse.fr/21011>

Official URL : <https://doi.org/10.1007/s11214-018-0523-4>

To cite this version :

Hurley, J. and Murdoch, Naomi and Teanby, N. A. and Bowles, N. and Warren, T. and Calcutt, S. B. and Mimoun, David and Pike, W. T. Isolation of Seismic Signal from InSight/SEIS-SP Microseismometer Measurements. (2018) Space Science Reviews, 214 (5). 1-22. ISSN 0038-6308

Any correspondence concerning this service should be sent to the repository administrator:

tech-oatao@listes-diff.inp-toulouse.fr

Isolation of Seismic Signal from InSight/SEIS-SP Microseismometer Measurements

J. Hurley¹ · N. Murdoch² · N.A. Teanby³ · N. Bowles⁴ ·
T. Warren⁴ · S.B. Calcutt⁴ · D. Mimoun² · W.T. Pike⁵

Abstract The InSight mission is due to launch in May 2018, carrying a payload of novel instruments designed and tested to probe the interior of Mars whilst deployed directly on the Martian regolith and partially isolated from the Martian environment by the Wind and Thermal Shield. Central to this payload is the seismometry package SEIS consisting of two seismometers, which is supported by a suite of environmental/meteorological sensors (Temperature and Wind Sensor for InSight TWINS; and Auxiliary Payload Sensor Suite APSS). In this work, an optimal estimations inversion scheme which aims to decorrelate the short-period seismometer (SEIS-SP) signal due to seismic activity alone from the environmental signal and random noise is detailed, and tested on both simulated and Viking data. This scheme also applies a module to identify measurements contaminated by Single Event Phenomena (SEP). This scheme will be deployed as the pre-processing pipeline for all SEIS-SP data prior to release to the scientific community for analysis.

Keywords Mars · InSight · Seismometer · Decorrelation · Noise

✉ J. Hurley
jane.hurley@stfc.ac.uk

¹ STFC Rutherford Appleton Laboratory, Harwell Science and Innovation Campus, Didcot, OX11 0QX, UK

² ISAE-SUPAERO, Toulouse, France

³ School of Earth Sciences, University of Bristol, Queens Road, Bristol, BS8 1RJ, UK

⁴ Atmospheric, Oceanic & Planetary Physics, Department of Physics, Clarendon Laboratory, University of Oxford, Parks Road, Oxford, OX1 3PU, UK

⁵ Imperial College, London, UK

1 Introduction

1.1 InSight

The InSight (Interior Exploration using Seismic Investigations, Geodesy and Heat Transport) mission to Mars was selected by NASA in August 2012, under the framework of the DISCOVERY program. With a launch in May 2018, it will deploy the first geophysical observatory on Mars, providing scientific knowledge essential to understand the fundamental processes of telluric planet formation and evolution: an in-situ investigation of the interior of a truly Earth-like planet. To accomplish its objectives, a tightly focussed payload has been assembled: the Seismic Experiment for Interior Structure (SEIS) and the Heat Flow and Physical Properties Package (HP3) (Banerdt et al. 2012, 2013; Lognonne et al. 2015; Mimoun et al. 2012).

The InSight mission will use geophysics to explore the Martian interior using seismic and thermal measurements and rotational dynamics, providing information about the initial accretion of the planet, the formation and differentiation of its core and crust, and the subsequent evolution of the interior. Knowledge of Mars' geophysics feeds directly into our understanding of what processes formed the rocky planets; of which the current knowledge is limited to Earth and the moon. Unlike the Moon, Mars is large and complex enough to have undergone most of the processes that affected early Earth but has not undergone extensive plate tectonics or other major reworking that erased evidence of early events.

Mars seismic activity likely stems from faulting (due to stress-release from the crust as the interior cools; Golombek et al. 1992; Knapmeyer et al. 2006; Taylor 2014) and from meteorite impacts (Davis 1993; Teanby and Wookey 2011; Teanby 2015). Although it is expected to be ≈ 100 times less seismically active than Earth, it is thought to be still seismically active today, as evidenced (for example) by recent tracks in dust leading to boulders in HiRISE images near known faults (Roberts et al. 2012).

1.1.1 SEIS-SP

SEIS comprises of two independent, three-axis seismometers: an ultra-sensitive very broad band (VBB) oblique seismometer, and a miniature, short-period (SP) seismometer. Both are mounted on the LVL (a precision levelling structure) along with their respective signal preamplifier stages, within sealed, nitrogen-backfilled enclosures. Together, the VBB, SP, and LVL are deployed on the ground as an integrated package, isolated from weather by the WTS (wind and thermal shield). They are connected by a flexible cable tether to the EBOX (a set of electronic cards located inside the lander's thermal enclosure).

The SEIS-SP microseismometer represents the UK contribution to the InSight SEIS payload which is a three-axis microseismometer, using three microfabricated sensors which include monolithic in-plane silicon proof mass and folded-cantilever suspensions with electroplated coils and capacitive sensors which are connected through proximity electronics (via the tether) to the associated analogue feedback circuits within the EBOX. The SEIS-SP electronics are based upon circuits described in Pike et al. (2009, 2013), Pike and Standley (2011), Gu et al. (2011), Delahunty and Pike (2013), Delahunty and Pike (2014).

Each sensor head (Fig. 1) consists of the sensor, a micromachined die package, surrounding magnetic assembly, proximity electronics and an encompassing hermetic package with connector to the tether harness: a 25 mm \times 25 mm micromachined silicon die bonded to further structures to complete the displacement transducer, and protect the sensor from damage due to shock and vibration. The silicon die contains the moving part of SEIS-SP, a moving

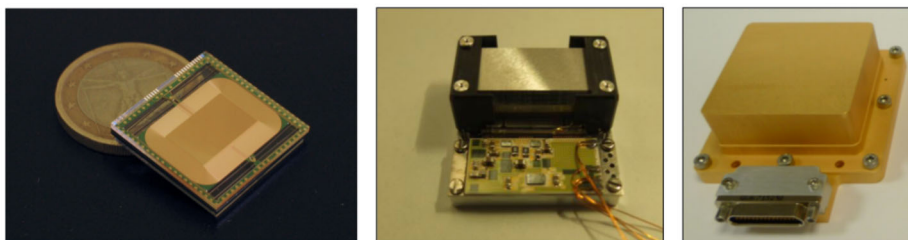


Fig. 1 The SEIS-SP die (left panel), with its proximity electronics (middle panel), mounted in its hermetic package with connector (right panel)

proof mass suspended within a stationary frame by a series of flexures. The proof mass is constrained to move in a single, compliant direction in the plane of the silicon die by the suspension design. The motion of the proof mass is measured capacitively using two sets of electrodes, a driving pair on the proof mass and a differential pick-up pair on a separate micromachined die, called the displacement transducer (DT). As the electrodes on the proof mass move with respect to the fixed electrodes on the DT, the overlap between the electrodes changes and the displacement can therefore be transduced. The magnetic assembly provides a static field perpendicular to the coil-current flow which together produces a Lorentz force to reposition the proof mass under electronic feedback control of the coil current. The assembly consists of a series of magnets, pole pieces and yokes to provide a closed magnetic circuit.

SEIS-SP is sensitive to frequencies between 0.05–40 Hz, recording data sampled at a rate of 100 Hz, and detects the acceleration of the ground along the sensitive axis along which the proof mass is free to move. The capacitive sensor detects the motion of the mass, operating under feedback control to increase the bandwidth and linearity, and to provide a velocity output. Thus, SEIS-SP does not model as a driven damped oscillator in the presence of an external force (such as those induced by the wind on the WTS) but rather as shown in Fig. 2.

On Mars, the deployed set-up will include the lander (lander body + solar panels, mounted on 3), the WTS (mounted on 3 feet) and SEIS (mounted on its 3 LVL feet). For the purposes of this work, the geometry of the lander, the WTS and SEIS instrument system are given in Fig. 3; the actual deployment geometry upon arrival on Mars is easily modifiable in the decorrelation pipeline. It is possible that the lander, WTS and SEIS may not be at the same vertical (z) height, as currently assumed.

It is usual that terrestrial seismometers are deployed in seismic vaults, in highly environmentally-controlled installations in which temperature, humidity, pressure and air-flow are known and stable, and in this way the recorded seismic measurements have reduced levels of environmental noise. For deployments in which vaults are not possible, the general approach involves installation of the seismometer, recording and analysis of installation-specific noise characteristics, and adjustment of the set-up in order to lower the overall noise levels—for instance, by mounting on sand. It is also common to bury sensors or to enclose sensors with an upturned container, when vaults are not possible, in order to mimic vault-like conditions. However, for SEIS, neither vault nor terrestrial empirical installation routes are possible, meaning that environmental noise (as well as the sought seismic activity) will be a ubiquitous part of whatever measurements are taken by SEIS on the surface of Mars. On Earth, there are also seismometers mounted on the ocean bottom, which similarly to SEIS, are not enclosed by vaults; it is possible, given suitable environmental sensors mounted on

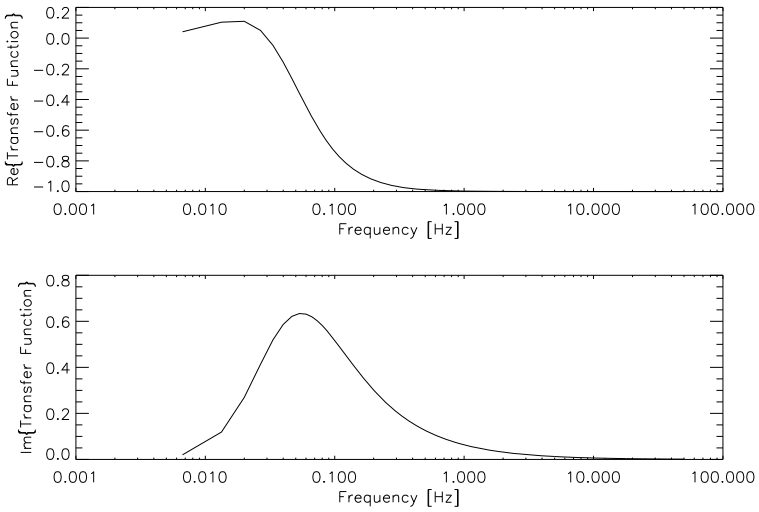
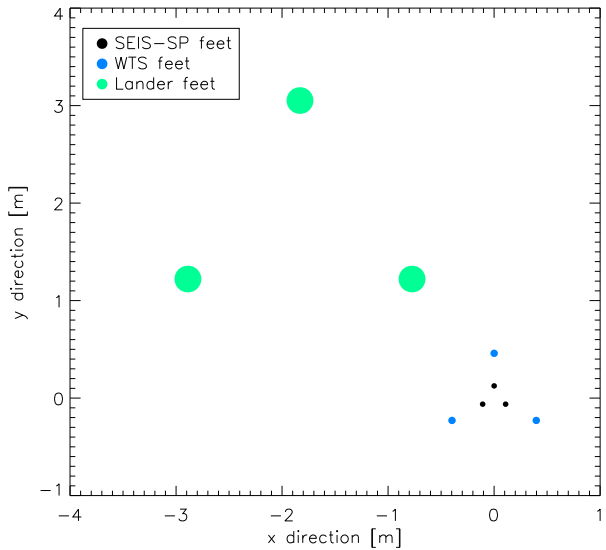


Fig. 2 The complex transfer function $T(s)$ for SEIS-SP in frequency space (s) (top = real component, bottom = imaginary component) as a function of frequency

Fig. 3 Assumed deployment geometry of the InSight lander and payload. The radii of the points used to represent the feet location are indicative of the specific foot radius



future ocean-bottom seismometers, that the decorrelation technique developed here could be applied to such seismometers

1.1.2 TWINS and APSS

As usual for lander and rovers, InSight has a suite of environmental sensors, called the APSS (Auxiliary Payload Sensor Suite) to complement the main scientific payload (SEIS and HP3). The APSS consists of a magnetometer, a pressure sensor, and a wind and temperature sensor (TWINS). The pressure sensor will measure at 2 Hz in nominal mode and

20 Hz in high-rate mode; the wind and temperature sensors will measure at 0.1 Hz and 1 Hz in nominal and high-rate modes, respectively.

2 Environmental Noise Sources on SEIS

As SEIS will be deployed in the Martian surface, and though it will be protected from the environment by WTS, it is by no means isolated from the environment. Thus, it is expected that SEIS measurements will include “noise” from the environment (namely from pressure, temperature and wind fluctuations) which contaminate the seismic records sought by the mission science drivers. It is usual to capture data in a seismically- and environmentally-quiet period to establish a quiet baseline which can be used to isolate seismic signals alone; however, this method requires accurate knowledge that the baseline is indeed quiet, that the measurements are additive, and does not allow for knowledge of the intrinsic errors in seismometer nor environmental sensor data. The scheme presented here allows for any dataset to be inverted without need for a quiet baseline dataset for comparison, and incorporates measurement errors and correlations into the isolation of the seismic signal from the random noise and environmental noise sources.

Murdoch et al. (2017) and Mimoun et al. (2017) have formulated and validated a model deriving the forces imparted to the SEIS-VBB (and hence the SEIS-SP) by wind and temperature variations via various possible pathways; their model also includes a module on pressure variations and their pathways through to the seismometer signals from Lognonné and Mosser (1993). This model is implemented in this work as the forward model \mathbf{f} , and is described qualitatively in Sects. 2.1–2.3; for details, please see Murdoch et al. (2017). Additionally, the environmental noise forward modelling from Murdoch et al. (2017) implemented in this work has also been implemented in Clinton et al. (2017).

Additionally, results from Teanby et al. (2017) on regolith inelastic coupling have been implemented in the modelling here, in conjunction with Murdoch’s regolith model; their results show that only a factor of 0.02 of the force transfers through a Mars-analogue regolith, due to inelastic losses.

Finally, a single event detection module has been included and implemented, which will filter spurious readings stemming from single event radiation on the SEIS-SP electronics, which is discussed in more detail in Sect. 2.4.

2.1 Wind

The wind field interacts with anything large on the surface of Mars, causing such objects to create disturbances which can be felt by the LVL feet which are then measured by the SEIS instruments; it is not possible to tell from what source the incoming disturbance signal comes when it arrives at the LVL feet and ultimately is measured by SEIS.

Though there may be other large features (such as boulders) on the surface nearby the deployment site, it is certain that the WTS itself and the lander will be sources of wind-induced disturbances. Sections 2.1.1 and 2.1.2 detail this pathway for WTS; it is identical for the lander.

2.1.1 Force of Wind on WTS

When wind is incident upon the WTS, it induces drag and lift forces onto the WTS. The WTS feet then exert forces on the regolith due to translation and rotation: translational motion will always happen, and for the purposes of this work, is assumed to be felt at the Centre

of Pressure (CoP) of the WTS; rotational motion will result when the line of action of the force does not pass directly through the Centre of Rotation (CoR) of the WTS. These forces are then transferred to the regolith via the WTS feet—for the purposes of this work, we assume that each foot takes one third of the total force on the WTS as a whole.

2.1.2 *Transfer Through Regolith*

The regolith model assumes a fully elastic half-space (defined only for the positive vertical direction, along with all horizontal directions) with properties of the regolith assumed as in Murdoch et al. (2017). Using a Green's tensor, the force from the disturbance from each WTS foot can be propagated through the regolith to the LVL feet, such that the ground deformation as a function of time can be estimated. The vertical component of this force then results in each LVL foot causing an indentation in the regolith from which it is then possible to calculate the overall change in disturbance in the position of each of the LVL feet which is measured by SEIS—both by VBB and SP—as an acceleration from one timestep to the next registered by the seismometers.

However, results from Teanby et al. (2017) confirm that the regolith cannot be modelled as fully elastic, and suggests that a fraction $f_{\text{inelas}} = 0.02$ of the disturbance is actually transferred, due to inelastic losses.

2.1.3 *Due to Lander*

As discussed in Sects. 2.1.1–2.1.2, disturbances due to wind acting on the lander are also included: the mathematical derivation of which can be assessed by substituting lander parameters instead of WTS parameters throughout.

2.2 Temperature

Fluctuations in temperature cause disturbances in the registered signals measured by SEIS-SP. Firstly, the WTS and SEIS-SP act as a thermal filters with associated thermal transfer functions: any fluctuation in environmental temperature will pass through the filtering effect of the WTS, and then through the SEIS-SP box (which also acts as a filter to the temperature fluctuation) before encountering the SEIS-SP sensors themselves; this temperature effect is independent of the SEIS-SP transfer function. Secondly, environmental temperature fluctuations, having passed through the filter of the WTS protection, will also cause the individual LVL legs to expand/contract via thermoelastic expansion; this will cause a tilt in the plane of the three SEIS-SP axes, which will cause the components of the signal to be altered primarily as acceleration on the horizontal axes.

2.3 Pressure

Pressure fluctuations cause propagated accelerations caused by tilting into the SEIS-SP measurement chain. This is modelled using the low-frequency oscillation solution of Lognonné and Mosser (1993); the range of oscillations expected on Mars have been considered, and even for dust devils, the low-frequency solution should hold here.

2.4 Single Events

Single event phenomena (SEP) are caused when very energetic heavy ions (any ion having an atomic number $Z > 1$) and protons pass through semiconductor materials and deposit a charge. If this direct or indirect (through spallation) charge is sufficient, then a Single Event Effect—either destructive (Single Event Latchup SEL, Single Event Burnout SEB, Single Event Gate Rupture SEGR, etc.) or non-destructive (Single Event Transient SET, Single Event Upset SEU, etc.)—can occur. Galactic cosmic rays and solar particle events are sources of such ions/protons; and hence are concern for the InSight electronics both in cruise to Mars as well as in its deployed phase.

SEIS-SP's electronics are chosen such that it operates within the performance specification during and after exposure to the high-energy radiation environments as detailed by the mission's environmental specifications, with a Radiation Design Factor (RDF) of 1, such that:

- Temporary loss of function or loss of data shall be permitted provided that the loss does not compromise the subsystem/system's health, that full performance can be recovered rapidly, and that there is no time in the mission that the loss is mission-critical.
- Normal operation and function shall be restored via internal correction methods without external intervention in the event of an SEU.
- Fault traceability shall be provided in the telemetry stream to the greatest extent practical for all anomalies involving SEEs.

A transient single event effect on a particular component will result in a spurious signal in the output from the axes channel in which the component corresponds in the feedback electronics. The problem is whether these transients will cause signals which are differentiable from potential seismic signals. It is expected that SEP will occur a maximum of $O(1e^{-2})$ events/day, and more typically at a rate of $O(1e^{-5})$ events/day—so it is expected to be very rare that spurious signals from SEPs will be registered in SEIS-SP signals.

Unless one seismometer axis is perfectly aligned with the tilt of the seismometer—the probability of which is virtually nil—the transient can only affect one axis at a time. From an operational perspective, then, simple comparison of all three SEIS-SP axis channels together will identify what signals are seismic (i.e. those for which a disturbance in signal is seen in all three channels) and those which are a result of SEU transients/effects (i.e. disturbance in only one channel). Experience in terrestrial seismometry indicates that this is an effective way in which to identify spurious signals in different seismometer channels.

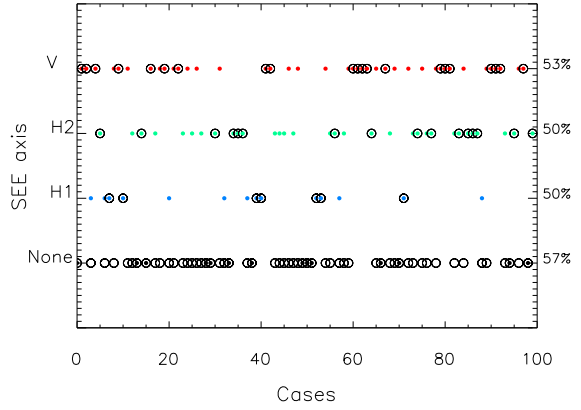
Thus, the SEP filtering module acts simply to run through each timestep of data signal \mathbf{y}_i measured by each of the three SEIS-SP axes i , comparing the timestep j with that immediately before, and using a simple threshold y_{thresh} , identifying large signals which are only evident in one axis:

$$\text{if } |\mathbf{y}_i(t_j) - \mathbf{y}_i(t_j - t_{j-1})| > y_{\text{thresh}} \quad \text{and} \quad \begin{cases} |\mathbf{y}_k(t_j) - \mathbf{y}_k(t_j - t_{j-1})| < y_{\text{thresh}} \\ |\mathbf{y}_m(t_j) - \mathbf{y}_m(t_j - t_{j-1})| < y_{\text{thresh}} \end{cases} \quad (1)$$

whereby $k, m \neq i$ and $k \neq m$, then there has been a SEP on axis i at timestep t_j . This timestep should then be disregarded from further analysis (Fig. 4).

This assertion is dependent upon the effect of all the SEPs being non-damaging to the components considered. It is thus worth assessing and monitoring the axes upon which an SEP has been identified to ensure that there is no change from its historical behaviour from timestep t_j onwards.

Fig. 4 Example of simulated SEP overlaid on top of SEIS-SP signal for SEIS-SP axes H1 in blue, H2 in green, V in red, and with SEP-detection module's identification of timing of detected SEP events and attribution of which axis is affected in larger black circles. Percentage of correct diagnoses per case (axis or no SEP event) highlighted by right vertical axis



3 Decorrelation Scheme: Optimal Estimations Inversion

Using the forward model \mathbf{f} described in the previous sections, an iterative optimal estimation method is employed to decorrelate the environmental signals from the total signal measured by the SEIS-SP sensors, in order to isolate the signal attributable only to seismic activity alone. This methodology is an application of that used in atmospheric science, whereby satellite spectra containing information upon temperature, pressure, chemical composition and any atmospheric phenomena such as aerosols and clouds are inverted in order to determine information on any one or more of these individual quantities. Due to the high recorded sampling rate of SEIS-SP measurements f_{SP} (of 100 Hz), inversions are run in discrete timebands Δt (usually around 2 s) consisting of $\Delta t f_{SP}$ individual timestep measurements (usually around 200) in the time-domain in order to keep array sizes manageable. The inversion scheme outlined below is applied for each defined timeband in the input SEIS-SP signal, and the results are concatenated together to provide the whole timeseries. This is based on the schemes in Rodgers (2000).

3.1 Inverted Parameters

The sought result of the decorrelation is the state vector \mathbf{x} in typical optimal estimations terminology: for the case at hand, it is the *force* attributable to the seismic signal alone, in xyz coordinates, and is defined as

$$\mathbf{x} = \begin{pmatrix} F(x_1) \\ F(x_2) \\ \vdots \\ F(x_N) \\ F(y_1) \\ F(y_2) \\ \vdots \\ F(y_N) \\ F(z_1) \\ F(z_2) \\ \vdots \\ F(z_N) \end{pmatrix} \quad (2)$$

for a timeband having N individual time-sampled measurements therein indexed by j , for force \mathbf{F} consisting of three perpendicular cartesian x_j , y_j , and z_j components. It should be noted that in the assumed deployment geometry, that these xyz coordinates correspond to north, east and vertical directions.

The measurement vector (from which the state vector is derived), then, is the *signal* \mathbf{S} measured directly from the three SEIS-SP axes, in SEIS-SP coordinates (H1, H2, V):

$$\mathbf{y} = \begin{pmatrix} S(H1_1) \\ S(H1_2) \\ \vdots \\ S(H1_N) \\ S(H2_1) \\ S(H2_2) \\ \vdots \\ S(H2_N) \\ S(V_1) \\ S(V_2) \\ \vdots \\ S(V_N) \end{pmatrix} \quad (3)$$

for a timeband having N individual time-sampled measurements therein indexed by j , for signal \mathbf{S} consisting of three SEIS-SP (non-perpendicular) axes components.

It should be noted here that whilst forces are additive, signals are not as they have been convolved through the SEIS-SP transfer function.

The Jacobian, \mathbf{K} , describes how the forward model \mathbf{f} varies with respect to the state vector $\frac{\partial \mathbf{f}}{\partial \mathbf{x}}$ —and essentially advises the step-direction of the iterative inversion process—calculated in this implementation by finite differences. It captures the change in signal at times i through j when each timestep i through j in the retrieval vector \mathbf{x} force is perturbed by Δx , such that $\partial x_i = (x_1 + \Delta x) - x_i$. Here:

$$\mathbf{K} = \begin{pmatrix} \frac{\partial \mathbf{f}_{H1_1}}{\partial x_1} & \frac{\partial \mathbf{f}_{H1_2}}{\partial x_1} & \dots & \frac{\partial \mathbf{f}_{H1_N}}{\partial x_1} & \frac{\partial \mathbf{f}_{H2_1}}{\partial x_1} & \frac{\partial \mathbf{f}_{H2_2}}{\partial x_1} & \dots & \frac{\partial \mathbf{f}_{H2_N}}{\partial x_1} & \dots & \frac{\partial \mathbf{f}_{V_1}}{\partial x_1} & \frac{\partial \mathbf{f}_{V_2}}{\partial x_1} & \dots & \frac{\partial \mathbf{f}_{V_N}}{\partial x_1} \\ \frac{\partial \mathbf{f}_{H1_1}}{\partial x_2} & \frac{\partial \mathbf{f}_{H1_2}}{\partial x_2} & \dots & \frac{\partial \mathbf{f}_{H1_N}}{\partial x_2} & \frac{\partial \mathbf{f}_{H2_1}}{\partial x_2} & \frac{\partial \mathbf{f}_{H2_2}}{\partial x_2} & \dots & \frac{\partial \mathbf{f}_{H2_N}}{\partial x_2} & \dots & \frac{\partial \mathbf{f}_{V_1}}{\partial x_2} & \frac{\partial \mathbf{f}_{V_2}}{\partial x_2} & \dots & \frac{\partial \mathbf{f}_{V_N}}{\partial x_2} \\ \dots & \dots & \dots & \dots & \dots & \dots & \dots & \dots & \dots & \dots & \dots & \dots & \dots \\ \frac{\partial \mathbf{f}_{H1_1}}{\partial x_N} & \frac{\partial \mathbf{f}_{H1_2}}{\partial x_N} & \dots & \frac{\partial \mathbf{f}_{H1_N}}{\partial x_N} & \frac{\partial \mathbf{f}_{H2_1}}{\partial x_N} & \frac{\partial \mathbf{f}_{H2_2}}{\partial x_N} & \dots & \frac{\partial \mathbf{f}_{H2_N}}{\partial x_N} & \dots & \frac{\partial \mathbf{f}_{V_1}}{\partial x_N} & \frac{\partial \mathbf{f}_{V_2}}{\partial x_N} & \dots & \frac{\partial \mathbf{f}_{V_N}}{\partial x_N} \\ \frac{\partial \mathbf{f}_{H1_1}}{\partial y_1} & \frac{\partial \mathbf{f}_{H1_2}}{\partial y_1} & \dots & \frac{\partial \mathbf{f}_{H1_N}}{\partial y_1} & \frac{\partial \mathbf{f}_{H2_1}}{\partial y_1} & \frac{\partial \mathbf{f}_{H2_2}}{\partial y_1} & \dots & \frac{\partial \mathbf{f}_{H2_N}}{\partial y_1} & \dots & \frac{\partial \mathbf{f}_{V_1}}{\partial y_1} & \frac{\partial \mathbf{f}_{V_2}}{\partial y_1} & \dots & \frac{\partial \mathbf{f}_{V_N}}{\partial y_1} \\ \frac{\partial \mathbf{f}_{H1_1}}{\partial y_2} & \frac{\partial \mathbf{f}_{H1_2}}{\partial y_2} & \dots & \frac{\partial \mathbf{f}_{H1_N}}{\partial y_2} & \frac{\partial \mathbf{f}_{H2_1}}{\partial y_2} & \frac{\partial \mathbf{f}_{H2_2}}{\partial y_2} & \dots & \frac{\partial \mathbf{f}_{H2_N}}{\partial y_2} & \dots & \frac{\partial \mathbf{f}_{V_1}}{\partial y_2} & \frac{\partial \mathbf{f}_{V_2}}{\partial y_2} & \dots & \frac{\partial \mathbf{f}_{V_N}}{\partial y_2} \\ \dots & \dots & \dots & \dots & \dots & \dots & \dots & \dots & \dots & \dots & \dots & \dots & \dots \\ \frac{\partial \mathbf{f}_{H1_1}}{\partial y_N} & \frac{\partial \mathbf{f}_{H1_2}}{\partial y_N} & \dots & \frac{\partial \mathbf{f}_{H1_N}}{\partial y_N} & \frac{\partial \mathbf{f}_{H2_1}}{\partial y_N} & \frac{\partial \mathbf{f}_{H2_2}}{\partial y_N} & \dots & \frac{\partial \mathbf{f}_{H2_N}}{\partial y_N} & \dots & \frac{\partial \mathbf{f}_{V_1}}{\partial y_N} & \frac{\partial \mathbf{f}_{V_2}}{\partial y_N} & \dots & \frac{\partial \mathbf{f}_{V_N}}{\partial y_N} \\ \frac{\partial \mathbf{f}_{H1_1}}{\partial z_1} & \frac{\partial \mathbf{f}_{H1_2}}{\partial z_1} & \dots & \frac{\partial \mathbf{f}_{H1_N}}{\partial z_1} & \frac{\partial \mathbf{f}_{H2_1}}{\partial z_1} & \frac{\partial \mathbf{f}_{H2_2}}{\partial z_1} & \dots & \frac{\partial \mathbf{f}_{H2_N}}{\partial z_1} & \dots & \frac{\partial \mathbf{f}_{V_1}}{\partial z_1} & \frac{\partial \mathbf{f}_{V_2}}{\partial z_1} & \dots & \frac{\partial \mathbf{f}_{V_N}}{\partial z_1} \\ \frac{\partial \mathbf{f}_{H1_1}}{\partial z_2} & \frac{\partial \mathbf{f}_{H1_2}}{\partial z_2} & \dots & \frac{\partial \mathbf{f}_{H1_N}}{\partial z_2} & \frac{\partial \mathbf{f}_{H2_1}}{\partial z_2} & \frac{\partial \mathbf{f}_{H2_2}}{\partial z_2} & \dots & \frac{\partial \mathbf{f}_{H2_N}}{\partial z_2} & \dots & \frac{\partial \mathbf{f}_{V_1}}{\partial z_2} & \frac{\partial \mathbf{f}_{V_2}}{\partial z_2} & \dots & \frac{\partial \mathbf{f}_{V_N}}{\partial z_2} \\ \dots & \dots & \dots & \dots & \dots & \dots & \dots & \dots & \dots & \dots & \dots & \dots & \dots \\ \frac{\partial \mathbf{f}_{H1_1}}{\partial z_N} & \frac{\partial \mathbf{f}_{H1_2}}{\partial z_N} & \dots & \frac{\partial \mathbf{f}_{H1_N}}{\partial z_N} & \frac{\partial \mathbf{f}_{H2_1}}{\partial z_N} & \frac{\partial \mathbf{f}_{H2_2}}{\partial z_N} & \dots & \frac{\partial \mathbf{f}_{H2_N}}{\partial z_N} & \dots & \frac{\partial \mathbf{f}_{V_1}}{\partial z_N} & \frac{\partial \mathbf{f}_{V_2}}{\partial z_N} & \dots & \frac{\partial \mathbf{f}_{V_N}}{\partial z_N} \end{pmatrix} \quad (4)$$

3.2 Errors

Errors on the measurements \mathbf{y} are accounted for in the measurement covariance matrix \mathbf{S}_y which is, in this case, a $3N$ -by- $3N$ diagonal matrix having diagonal elements equal to the square of the standard deviation of the random noise, σ_y , believed to occur on each SEIS-SP signal timestep, such that

$$\mathbf{S}_y = \begin{pmatrix} \sigma_{y_{H1}}^2 \mathbf{I}_N & \cdots & \cdots \\ \cdots & \sigma_{y_{H2}}^2 \mathbf{I}_N & \cdots \\ \cdots & \cdots & \sigma_{y_V}^2 \mathbf{I}_N \end{pmatrix} \quad (5)$$

where \mathbf{I}_M is the N -by- N identity matrix. The value of $\sigma_{y_{H1}}$ and $\sigma_{y_{H2}}$, and σ_{y_V} for the SEIS-SP design parameters are $1e^{-9}$ m/s²/Hz^{1/2} and $5e^{-8}$ m/s²/Hz^{1/2}, respectively, estimated at 1 Hz.

3.3 Iterative Formulation and Error Propagation

An iterative form of optimal estimation is used in order to numerically converge to a solution. Starting at $i = 0$ with the first guess $\mathbf{x}_0 = \mathbf{a}$, the iterative state vector is defined as

$$\mathbf{x}_{i+1} = \mathbf{x}_i + [(1.0 + \gamma)\mathbf{S}_a^{-1} + \mathbf{K}_i^T \mathbf{S}_y^{-1} \mathbf{K}_i]^{-1} [\mathbf{K}_i^T \mathbf{S}_y^{-1} (\mathbf{y} - \mathbf{f}_i) + \mathbf{S}_a^{-1} (\mathbf{x}_i - \mathbf{a})] \quad (6)$$

where \mathbf{S}_a is the a priori covariance which is described in detail in Sect. 3.4, and γ is the Levenberg-Marquardt parameter which can take any finite value and that acts to adjust the iterative “step-size” in order to maintain monotonic progress towards the solution of lowest least squares error (Rodgers 2000). This least squares error is a metric of the difference between the measurements and the estimate of the measurements via the forward model for each iteratively determined inversion vector, and is quantified by the χ^2 error, defined as

$$\chi_{i+1}^2 = \frac{1}{N} [(\mathbf{y} - \mathbf{f}_i)^T \mathbf{S}_y^{-1} (\mathbf{y} - \mathbf{f}_i) + (\mathbf{x}_i - \mathbf{a}) \mathbf{S}_a^{-1} (\mathbf{x}_i - \mathbf{a})] \quad (7)$$

which should approach unity for a fit that is consistent with the measurements. The error in the inverted parameters themselves thus calculated is expressed as the error covariance matrix \mathbf{S}_x

$$\mathbf{S}_x = (\mathbf{K}_i^T \mathbf{S}_y^{-1} \mathbf{K}_i + \mathbf{S}_a^{-1})^{-1}. \quad (8)$$

Typically, the difference between two iterative values of χ^2 determines when the optimal estimation inversion is said to converge—when $\chi_{i+1}^2 - \chi_i^2 \rightarrow 0$, the inversion is said to have converged—here when $\frac{\chi_{i+1}^2 - \chi_i^2}{\chi_i^2} \times 100\% \leq 0.1\%$.

3.4 A Priori

As it is an optimal estimation scheme that is implemented, an a priori state vector \mathbf{a} must be provided to bound the possible inverted values—and in this implementation, this a priori is taken as the first guess of the inverted state vector \mathbf{x} in the iterative inversion process. A pessimistic a priori could be taken that there is no seismic activity (thus $\mathbf{a} = 0$); however, inversion of the measurements can provide a better starting point.

3.4.1 A Priori Preliminary Inversion

When starting a decorrelation, the analyst has the SEIS-SP measured signal and the TWINS/APSS metrological data available. However, he does not know how much of the measured signal is attributable to seismic vs. aseismic components—and in any case, the seismic and aseismic sources are not additive.

Unlike the signals, the measured force and attributable environment forces are additive, and can be subtracted in order to yield the a priori force attributable to the seismic activity alone:

$$\mathbf{a} = \mathbf{y}_{\text{force}} - \mathbf{x}_{\text{env}} \quad (9)$$

However, $\mathbf{y}_{\text{force}}$ and \mathbf{x}_{env} are not readily available without some estimation.

Taking the environmental pseudo-a priori data (wind, pressure and temperature) from APSS/TWINS, and running these through the forward model \mathbf{f} provides the force attributable to the environment factors alone in xyz coordinates \mathbf{x}_{env} .

The measured signal \mathbf{y} in SEIS-SP-axes coordinates (H1, H2 and V) can then be used in a preliminary inversion to convert the signal into measured force in xyz coordinates $\mathbf{y}_{\text{force}}$. In this preliminary inversion, which is run for each SEIS-SP axes individually, the signal as a function of time for each SEIS-SP axes is converted into the force for each SEIS-SP axes $x_{\text{prel}}(t)$ as a function of time. This is accomplished by defining a preliminary inversion forward model f_{prel} such that

$$y = x(t) * T(t) \quad (10)$$

whereby $y(t)$ is the signal measured by each SEIS-SP axes, which is defined by the force as a function of time $x(t)$ convolved with the complex SEIS-SP transfer function $T(t)$ which itself has been converted from its frequency domain $T(s)$ into the time domain $T(t)$.

This preliminary inversion uses the same iterative formulation defined in Eq. (6); it thus requires an preliminary a priori $a_{\text{prel}}(t)$ which is taken here to be $\mathbf{1}$, and error estimates on both the preliminary a priori and the measurement used in the preliminary retrieval ($y_{\text{prel}}(t) = y(t)$ from the main decorrelation inversion) which are taken to be $\sigma_{x_{\text{prel}}} = 1$, $\sigma_{y_{\text{prel}}} = 0.1$. It also requires preliminary covariance matrices $\mathbf{S}_{a_{\text{prel}}} = \sigma_{x_{\text{prel}}}^2 \mathbf{1}$ and $\mathbf{S}_{y_{\text{prel}}} = \sigma_{y_{\text{prel}}}^2 \mathbf{1}$.

This iterative preliminary retrieval is then let run until it converges for the inverted state vector \mathbf{x}_{prel} , which is said to happen when χ^2 is below 0.001 or the difference between two consecutive iterative χ^2 values is less than 0.001.

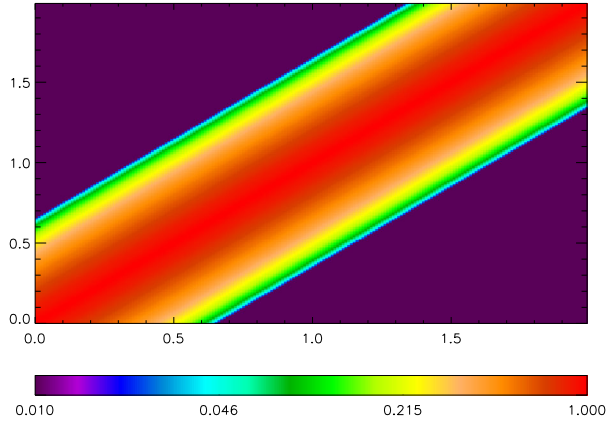
Once inverted, the estimated forces $x_{\text{prel}}(t)$ are combined into vector form (whereby there are N values for each of the 3 SEIS-SP axes H1, H2 and V), and rotated from SP axes coordinates (H1, H2 and V) to xyz coordinates such that

$$\mathbf{y}_{\text{force}} = \begin{pmatrix} x_{\text{prel}H1} \\ \sqrt{x_{\text{prel}H1}^2 - x_{\text{prel}H2}^2} \cos^2 \theta / \sin^2 \theta \\ x_{\text{prel}V} \end{pmatrix} \quad (11)$$

whereby $\theta = 60^\circ$.

This $\mathbf{y}_{\text{force}}$ and \mathbf{x}_{env} can then be supplied to Eq. (9) to estimate the a prior for the decorrelation.

Fig. 5 Example a priori covariance matrix \mathbf{S}_a for HI over a 2 second timeband, showing correlation (0 to 1) between timesteps



3.4.2 Implementation of a Priori in Decorrelation

The inversion is allowed to vary from the a priori forces in a manner proportional to the uncertainty σ_a in \mathbf{a} , which is specified for each of the xyz coordinates. Typically, σ_a is taken to be the variance of expected inverted values; in this case, this is defined for each of the three xyz coordinates: $\sigma_{a_x} = 3e^{-8} \text{ m/s}^2/\text{Hz}^{\frac{1}{2}}$, $\sigma_{a_y} = 6e^{-8} \text{ m/s}^2/\text{Hz}^{\frac{1}{2}}$ and $\sigma_{a_z} = 2e^{-7} \text{ m/s}^2/\text{Hz}^{\frac{1}{2}}$, estimated at 1 Hz. This is accounted for in the $3N$ -by- $3N$ a priori covariance matrix \mathbf{S}_a , which includes correlations between different inverted variables—and to aid in obtaining a physically smooth inverted state vector, correlations between each sub-timestep within an inversion timeband are assumed via a linear correlation in time between 0 and 1 (Fig. 5):

$$\mathbf{S}_{a_{ij}} = \begin{pmatrix} (1 - \frac{|j-i|}{N})\sigma_{a_x}^2 \mathbf{I}_N & \dots & \dots \\ \dots & (1 - \frac{|j-i|}{N})\sigma_{a_y}^2 \mathbf{I}_N & \dots \\ \dots & \dots & (1 - \frac{|j-i|}{N})\sigma_{a_z}^2 \mathbf{I}_N \end{pmatrix} \quad (12)$$

Because the correlation is assumed over the timeband—which itself is generally taken to be about 1 s—but the data is taken at 100 Hz, this may limit the frequency content that can be recovered to lower-frequency seismograms. Thus, care should be taken to match the \mathbf{S}_a to the kind of signal that is being recovered in order to best capture the frequency of the noise and signal.

4 Application to Simulated Data

The performance and behaviour of optimal estimations decorrelation schemes are best tested using simulated data for which the “true” state is known, and in this case, the various simulated (and hence known) environmental noise sources can be added on in a controlled manner using the forward model. The applicability of the inversion to real data and assumed performance, of course then assumes that the forward model does a sufficient and representative job of representing reality, which cannot be quantified in these simulation tests, but is assessed in Murdoch et al. (2017).

To this end, simulated meteorological conditions as shown in Fig. 6 have been generated using representative magnitudes and timescales of variability from Murdoch et al. (2017).

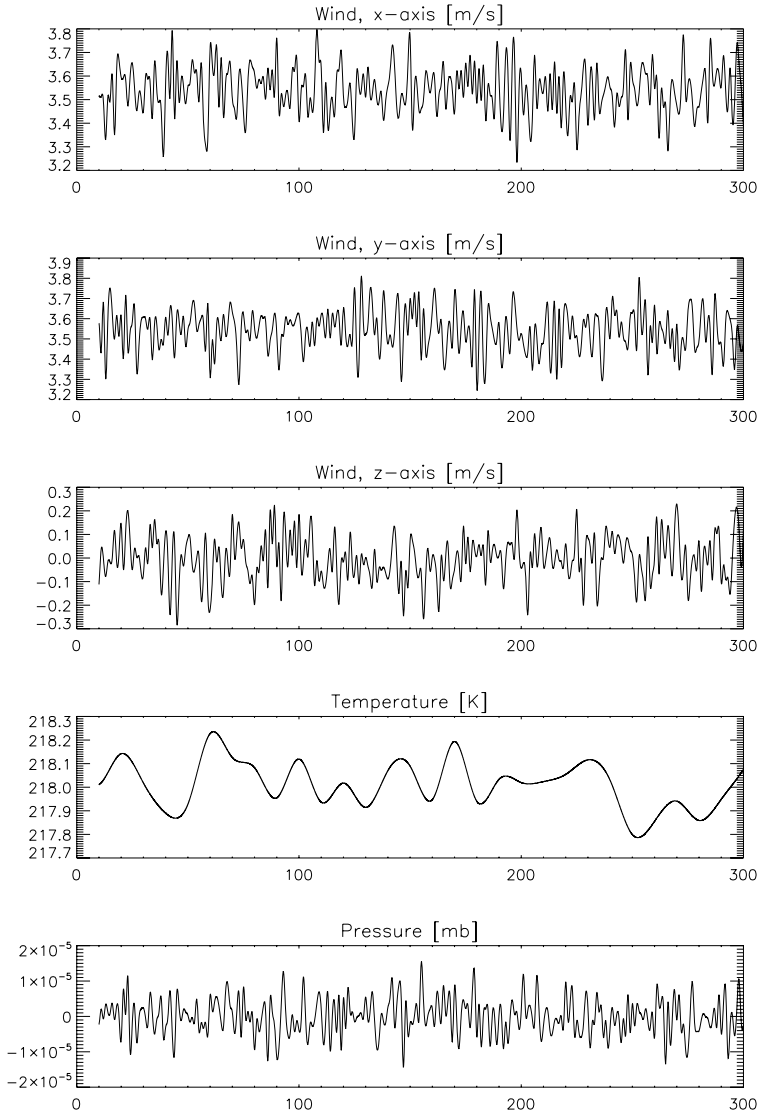


Fig. 6 Simulated meteorological conditions for example: top three panels are components of wind in xyz coordinates, fourth panel is temperature at ground level outside of the WTS, bottom panel is the pressure at ground level. Please note that example is 300 s long, and sampled at 100 Hz

They have been interpolated onto the frequencies of measurement of the nominal TWINS and APSS data capture mode.

The simulated seismic velocity measurement is taken from Teanby and Wookey (2011); representative of an explosive source at 50 km depth, rendering a total moment of 10^{17} Nm (magnitude 5.3) at a location 60° (≈ 3000 km) away from the assumed SEIS-SP location. This has then been resampled at the SEIS-SP frequency (100 Hz), and convolved with the SEIS-SP transfer function in order to simulate what SEIS-SP would measure in a noise-free and isolated set-up (Fig. 7 top two rows).

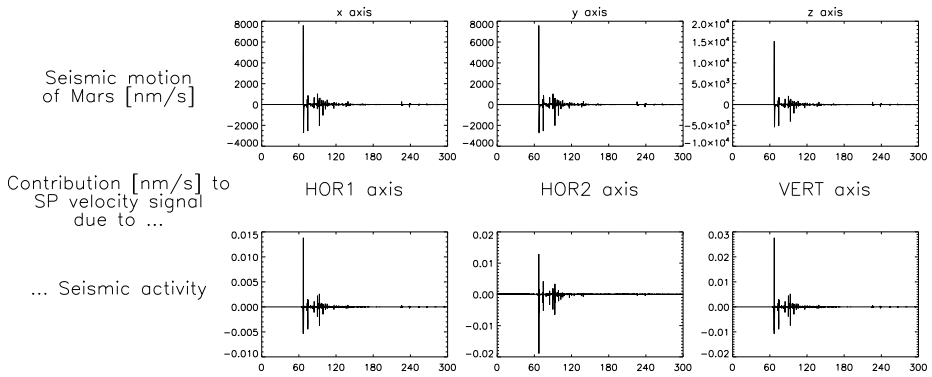


Fig. 7 Example simulation: the motion of Martian regolith in each xyz axis (top row), and the contribution to the total signal measured by each SEIS-SP axis (H1, H2, and V) due to the seismic motion (bottom row)

4.1 Detectability and Sensitivities to Environmental Parameters

The ability of the decorrelation scheme to identify and remove various components of signal is dependent upon the sensitivity of the measurements to show differential in signal in each axis above the level of expected noise; if the change in signal for a particular parameter is greater than this noise level, then the signal due to the parameter is detectable and removable. In standard optimal estimations theory, this is captured by the Jacobian matrix \mathbf{K} .

Figure 8 shows these sensitivities (i.e. change in signal corresponding to a change) for seismic forces in each of the xyz directions independently, for wind speeds in each of the xyz directions independently for both the WTS and lander interactions, for temperature fluctuations as fedthrough both the SEIS-SP transfer function and through thermoelastic tilt routes, and for fluctuations in pressure. Generally:

- SEIS-SP axes are very sensitive to the correlated xyz seismic signal, with some crossover in the horizontal axes as expected;
- All SEIS-SP axes are sensitive to the effects of wind on the WTS for wind speeds greater than ≈ 1 m/s;
- All SEIS-SP axes are sensitive to the effects of wind on the lander for wind speeds greater than $\approx 2\text{--}3$ m/s;
- The horizontal SEIS-SP axes are sensitive to all expected temperature fluctuations;
- Temperature and pressure fluctuations are not detectable through the SEIS-SP transfer function.

For the seismic example shown in Fig. 7 and the environmental series shown in Fig. 6, the components of signal attributable to each environmental noise source as a function of time are shown in Fig. 9. Note that whilst components of force are additive, the components of signal (which are convolved with the complex SEIS-SP transfer function) are not.

4.2 Extraction of Seismic Signal from Noisy Simulations

The simulated signal used to assess the overall performance and ability of the optimal estimations decorrelation is obtained by running the forward model with the simulated meteorological conditions from Fig. 6 to obtain the individual force components (xyz) attributable

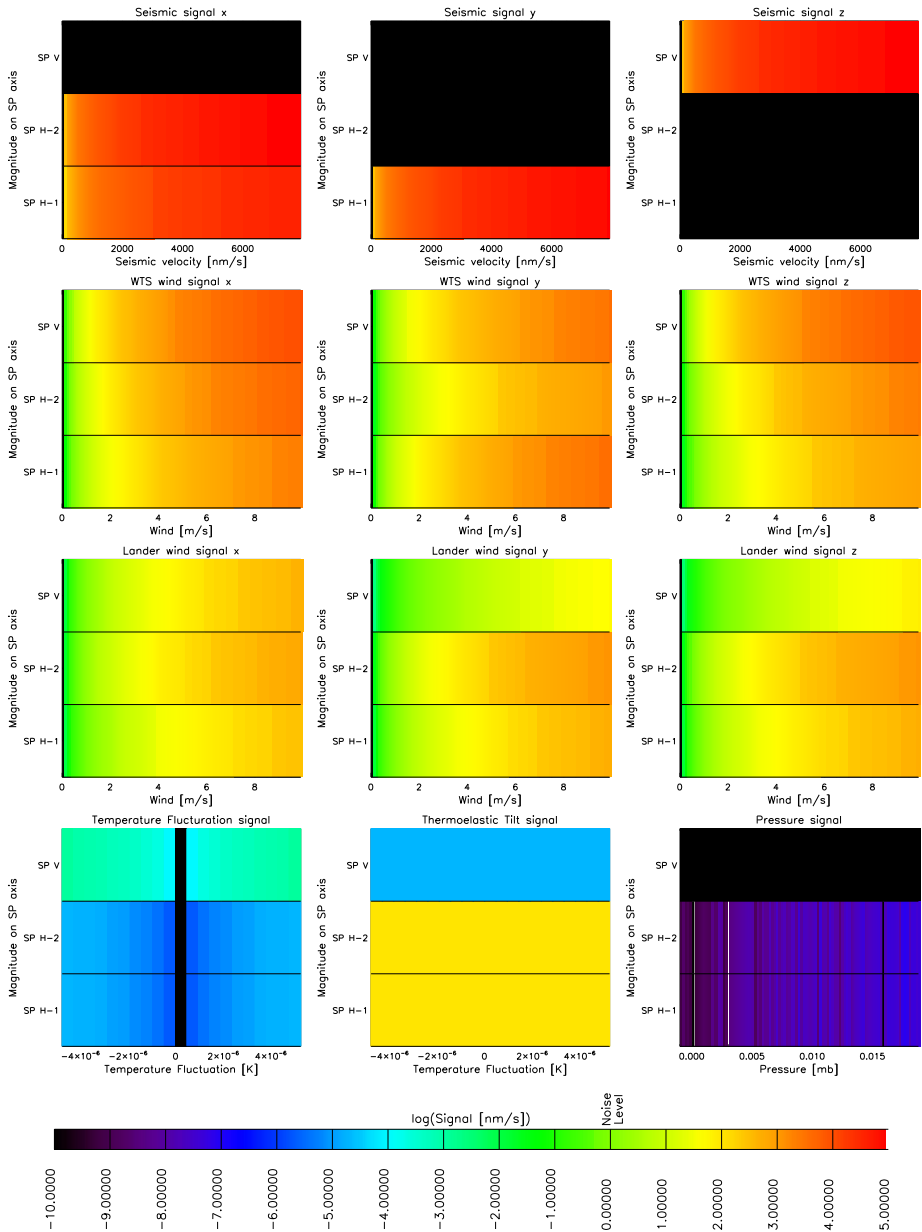


Fig. 8 Sensitivity of the SEIS-SP signal in SP axes (H1, H2, V; vertical axis of each panel) to strength of an imposed seismic signal applied in xyz direction (top row, each panel a different xyz axis), and to varying environmental conditions: second row is due to wind on the WTS (each panel for wind in a different xyz direction), third row is due to wind on the lander (each panel for wind in a different xyz direction), fourth row left panel is due to temperature fluctuations, middle panel is due to thermoelastic tilt and right panel is due to pressure fluctuations

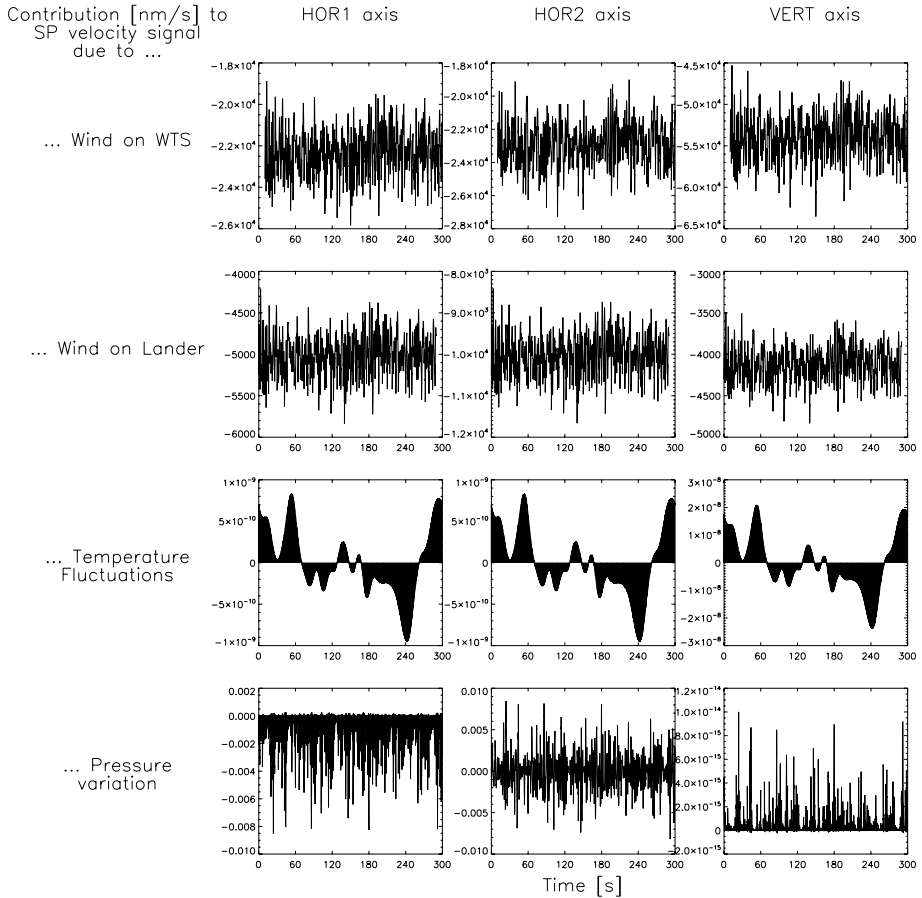


Fig. 9 Example simulation: the contribution to the total signal measured by each SEIS-SP axis (H1, H2, and V) due to the wind on the WTS (first row) and lander (second row), the temperature fluctuations (third row), the thermoelastic tilt (fourth row), the pressure variation (last row). The wind, temperature and pressure time-series used in this example simulation are shown in Fig. 6

to each environmental noise source, combining these with the seismic force (xyz) components, and then convolving these forces through the SEIS-SP transfer function to obtain the overall signal registered in each of the SEIS-SP axes (H1, H2, and V). Next random noise is added on top of each of the SEIS-SP axes signal time-series, with magnitude of each random distribution of noise corresponding to σ_y for each axis. The blue lines in the first and third rows of Fig. 10 show the simulated “noisy” velocity (i.e. force) in xyz and signal in H1/H2/V axes; the red line shows the “pure” signal—that is, the seismic “truth” signal for which the decorrelation is ultimately aiming from starting the optimal estimations inversion at the “noisy” input signal and the meteorological data.

The optimal estimations scheme is then applied to this “noisy” input signal, and the inversion allowed to iterate until convergence is achieved, over the full 300 s timeseries in discrete timebands of 2 s; the results of which are shown in Fig. 10 in both the velocity and signal time-domains. Looking at the difference plots in the second and fourth row, the impact of the environmental noise (as opposed to the noise-free “pure” signal) is clearly

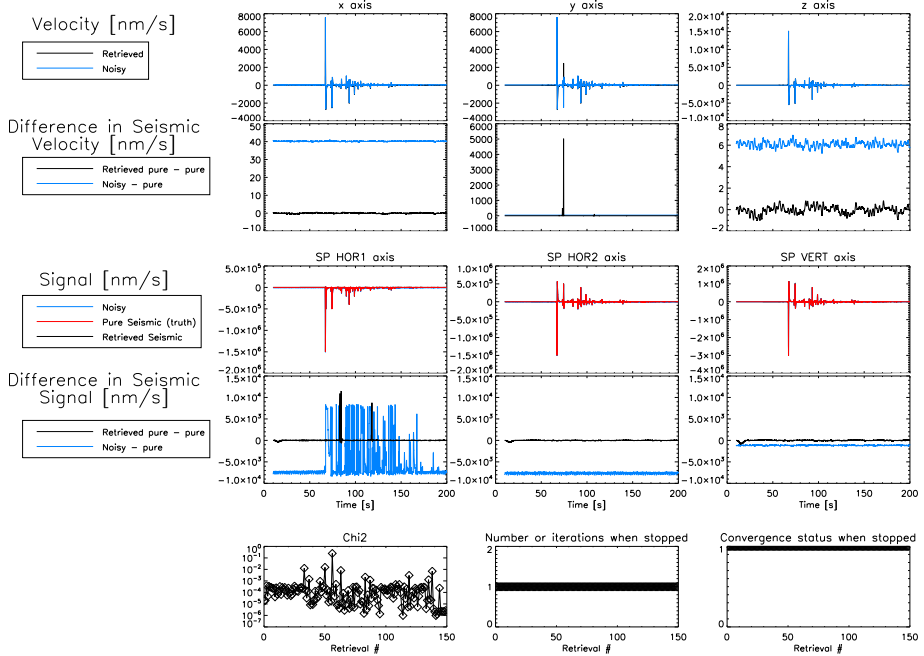


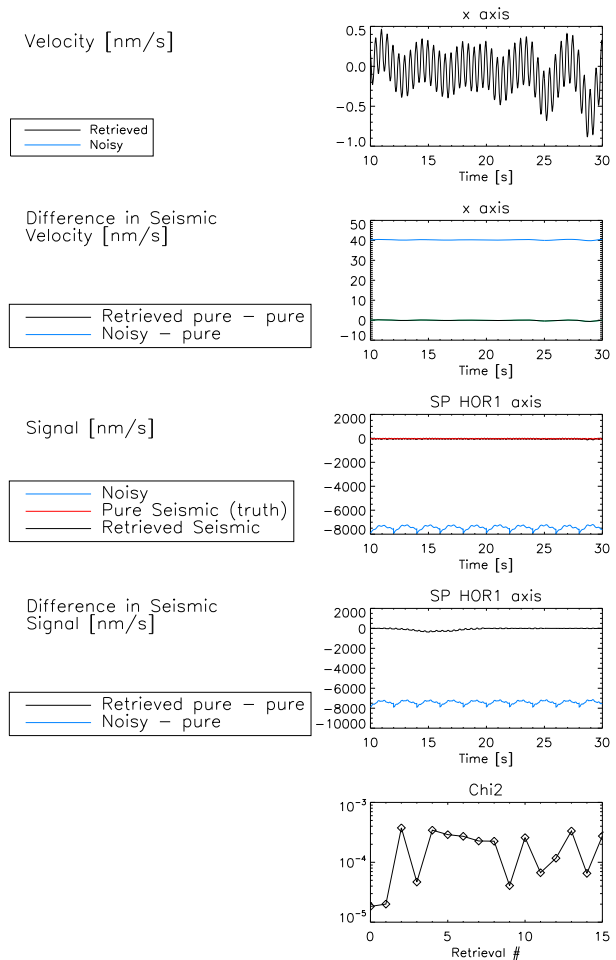
Fig. 10 Result of application of optimal estimations scheme to example seismic signal contaminated with example environmental inputs: top row shows the inverted (black) and noisy (blue) velocity in xyz axes; second row shows the difference between the inverted and pure seismic-signal-along velocity (black), between the noisy and pure seismic-signal-along velocity (blue) in the xyz axes; third and fourth row show the same plots, but in the signal measured in the SEIS-SP H1, H2 and V axes; the final row shows the χ^2 error (left panel), the number of iterations required for convergence (middle row) and the convergence status (right panel; 0 = unconverged, 1 = converged) in each of the 2 s-long timebands in which the total time series has been inverted

visible—for instance, it is a nearly uniform offset of 40 nm/s in velocity in the x direction (this is the dominant wind impact), with more structure visible in the H1 SP axes signal plot. Looking at the velocities and signals inverted from the optimal estimations scheme, the difference between the “pure” and the inverted noise-free signal is largely zero, with a couple of notable exceptions when there is information missing on the horizontal axes (x/y vs. H1/H2) which are not always distinguishable. Fig. 11 shows a only the x and SP-H1 axis, over the first 30 s, for ease of viewing. Thus, it is clear that the optimal estimations inversion is capable of differentiating between environmental noise and seismic signals, assuming that the forward model properly represents the environmental forces. Looking at convergence parameters, for this simulated example, the scheme converges within two iterations, with a low cost function value, as quantified by the χ^2 value.

4.3 Sensitivities and Operational Considerations

Environmental noise is present continuously, and is ubiquitous on any signal recorded. However, the SEIS-SP signal is recorded at a particular frequency, the various environmental monitoring signals at other frequencies; and the scheme’s ability to decorrelate the environmental signal will be influenced by the relationship between these as well as the frequency of fluctuation of the environmental parameters themselves. In theory, the highest-possible

Fig. 11 As for Fig. 10, but just for the x and SP-H1 axis for the first 30 s of data



frequency data of concurrent SEIS-SP and APSS/TWINS measurements would give the best decorrelation; however, this is not the design case (SEIS-SP has nominal frequency of 100 Hz; APSS has nominal frequency of 2 Hz and high-rate mode of 20 Hz; TWINS has nominal frequency of 0.1 Hz and a high-rate mode of 1 Hz), nor is it operationally-reasonable to expect that such a high data rate is possible continuously. From a processing perspective, it is also advantageous to use the fewest number of datapoints (i.e. the lowest frequency) to increase the speed of the processing pipeline which decorrelates the environmental signal from the seismic signal.

During the commissioning phase when the lander is first deployed on the Martian surface, both high-rate and nominal mode APSS and TWINS measurements will be taken during expected noisy and less-noisy periods (day and night, respectively), which will be used to assess how the decorrelation performs with real data and environmental inputs.

Figure 12 shows the impact of varying the frequency at which the input APSS/TWINS pressure, temperature and wind-speed measurements are provided to the optimal estimation scheme on the inverted performance. In this investigation, environmental noise is applied via the forward model to each 100 Hz SEIS-SP frequency record; this yields the simulated

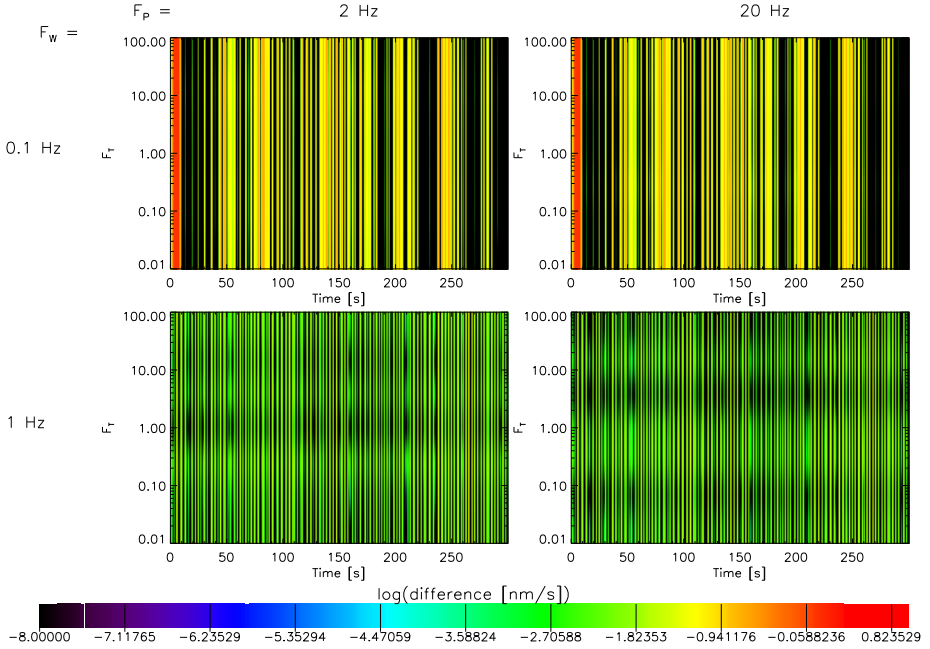


Fig. 12 Difference between the inverted and pure simulated noise-free velocity timeseries for example simulation when environmental information (namely temperature information, pressure information and wind information) is provided at different frequencies. Each panel shows a different combination of frequency of temperature information (F_T) for varying frequency of pressure information (F_P , each column) and frequency of wind information (F_W , each row), with the nominal operational mode frequencies for each highlighted in blue and high-frequency mode frequencies highlighted in red

time-series. Next, the scheme is run with pressure, temperature and wind-speed information provided at varying frequencies between 0.01–100 Hz. The frequency at which pressure is input within this range makes no difference to the performance of the inversion; similarly the rate of temperature information makes little difference; the inversion performance improves with increased frequency of the input wind-speed information, but makes little difference between nominal and high-rate TWINS modes. This implies that for environmental fluctuations having expected frequencies (i.e. not high-frequency perturbations like dust-devils), that both the nominal and high-rate modes should be sufficient to decorrelate the environmental noise from the seismic signal.

5 Application to Viking Data

The Viking Lander 2 seismometer captured data on Sol 80 at 03h00 of the Viking mission which has been asserted to be seismic in origin (of estimated magnitude 2.7), given interpolation on wind, pressure and temperature data taken around the time period of the event (Lorenz et al. 2016). This represents a good test case of a real Marsquake in the presence of environmental signal contamination, upon which to apply the scheme developed here.

The Viking 2 lander seismometer data was captured at a frequency of 1.01 Hz in 3 perpendicular axes; the metrology (wind, pressure and temperature) data was taken much less frequently with the closest data taken before the event at 02h40 and after the event at 03h45.

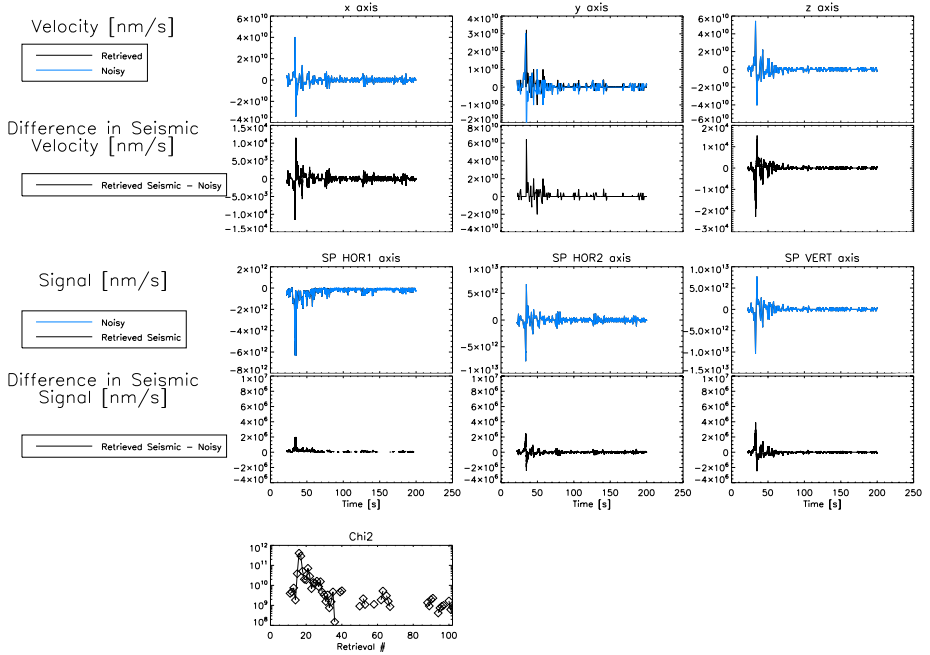


Fig. 13 Result of application of optimal estimations scheme to Viking Sol 80 signal, which implicitly contains environmental noise sources: top row shows the inverted (black) and noisy (blue) velocity in xyz axes; second row shows the difference between the inverted and Viking velocity (blue); third and fourth row show the same plots, but in the signal measured in the SEIS-SP H1, H2 and V axes; the final row shows the χ^2 error in each of the 2 s-long timebands in which the total time series has been inverted

For this experiment, the seismometer and metrology data is interpolated onto the SEIS-SP frequency, and the seismometer data convolved through the SEIS-SP transfer function. There is no further environmental nor random noise added to the seismometer data since it already includes components of both these errors sources. The optimal estimations scheme is then applied using these interpolated measurements as inputs, and the SEIS-SP forward model in order to isolate the portion of signal attributable to seismic sources alone—it is worth noting that because of the SEIS-SP parameters used here, that this will yield only a rough estimate of whether the signal measured is attributable to environmental sources or rather that it requires a seismic component of input in order to reach the signal measured. Figure 13 shows the results of this experiment; whilst there are clearly artefacts stemming from instrument-specific and regolith assumptions on the inverted values, the decorrelation scheme suggests that the large signal features are indeed attributable to non-environmental sources, taking out small magnitude components of signal which are probably attributable to environmental fluctuations.

6 Conclusions

An optimal estimations inversion has been developed using the forward model developed in Murdoch et al. (2017) in order to decorrelate seismic components of InSight SEIS-SP signal from environmental and random noise. Using simulated data and expected design noise

levels, the optimal estimations scheme is successful in detecting and removing signals from wind and temperature fluctuations, but pressure fluctuations are below the noise level. Application of the scheme to Viking data implies that the Viking 2 seismic event on sol 300 was indeed likely a seismic event, assuming all geophysical parameters and the forward model are representative. Analysis shows that nominal mode measurements are sufficient to decorrelate environmental signals from seismic, and that high-resolution mode measurements are not required except to invert low windspeeds or small temperature variations.

A SEP-identification module has been implemented as a preliminary filter to the decorrelation scheme; this has also proven capable of identifying timesteps in continuous data with single event contamination; a requirement of the InSight environmental requirements pertaining to radiation. This will be implemented as part of the operational processing; it is, however, expected that the raw data will also be provided to end users.

Future work includes field testing of test units of SEIS-SP packages modified for terrestrial use (i.e. g_{earth} vs. g_{mars}) in a representative unisolated installation in order to test the representativeness of the modelling and assumptions made. The scheme will also be applied to the simulated dataset in Clinton et al. (2017), which can be upsampled from 2 Hz.

Acknowledgements We acknowledge the UKSA Aurora framework for supporting the principal and several co-authors.

References

- W.B. Banerdt, S. Smrekar, L. Alkalai, T. Hoffman, R. Warwick, K. Hurst, W. Folkner, P. Lognonne, T. Spohn, S. Asmar, D. Banfield, L. Boschi, U. Christensen, V. Dehant, D. Giardini, W. Goetz, M. Golombek, M. Grott, T. Hudson, C. Johnson, G. Kargl, N. Kobayashi, J. Maki, D. Mimoun, A. Mocquet, P. Morgan, M. Panning, J. Pike Tromp, T. van Zoest, R. Weber, M. Wieczorek (The Insight Team), InSight: an integrated exploration of the interior of Mars, in *Lunar and Planetary Science Conference*. Lunar and Planetary Inst. Technical Report, vol. 43 (2012), p. 2838
- W.B. Banerdt, S. Smrekar, P. Lognonne, T. Spohn, S.W. Asmar, D. Banfield, L. Boschi, U. Christensen, V. Dehant, W. Folkner, D. Giardini, W. Goetze, M. Golombek, M. Grott, T. Hudson, C. Johnson, G. Kargl, N. Kobayashi, J. Maki, D. Mimoun, A. Mocquet, P. Morgan, M. Panning, W.T. Pike, J. Tromp, T. van Zoest, R. Weber, M.A. Wieczorek, R. Garcia, K. Hurst, InSight: a discovery mission to explore the interior of Mars, in *Lunar and Planetary Science Conference*. Lunar and Planetary Inst. Technical Report, vol. 44 (2013), p. 1915
- J.F. Clinton, D. Giardini, P. Lognonne, B. Banerdt, M. van Driel, M. Drilleau, N. Murdoch, M. Panning, R. Garcia, D. Mimoun, M. Golombek, J. Tromp, R. Weber, M. Bose, S. Ceylan, I. Daubar, B. Kenda, A. Khan, L. Perrin, A. Spiga, Preparing for InSight: an invitation to participate in a blind test for Martian seismicity. *Seismol. Res. Lett.* **88**(5), 1290–1302 (2017). <https://doi.org/10.1785/0220170094>
- P.M. Davis, Meteoroid impacts as seismic sources on Mars. *Icarus* **105**, 469–478 (1993)
- A. Delahunty, W.T. Pike, Integrating solder bumpers for high shock applications, in *Proc. IEEE MEMS Conf. 2013*, Tapei, Jan 20–24 (2013), pp. 689–692
- A.K. Delahunty, W.T. Pike, Metal-armouring for shock protection of MEMS. *Sens. Actuators A* **215**, 36–43 (2014)
- M.P. Golombek, W.B. Banerdt, K.L. Tanaka, D.M. Tralli, A prediction of Mars seismicity from surface faulting. *Science* **258**, 979–981 (1992)
- J. Gu, W.T. Pike, W.J. Karl, Solder pump for through-wafer vias. *J. Microelectromech. Syst.* **20**, 561–563 (2011)
- M. Knapmeyer, J. Oberst, E. Hauber, M. Wahlisch, C. Deuchler, R. Wagner, Working models for spatial distribution and level of Mars' seismicity. *J. Geophys. Res.* **111**, 11006 (2006)
- P. Lognonné, B. Mosser, Planetary seismology. *Surv. Geophys.* **14**, 239–302 (1993)
- P. Lognonne, W.B. Banerdt, R.C. Weber, D. Giardini, W.T. Pike, U. Christensen, D. Mimoun, J. Clinton, V. Dehant, R. Garcia, C. Johnson, N. Kobayashi, B. Knapmeyer-Endrun, A. Mocquet, M. Panning, S. Smrekar, J. Tromp, M. Wieczorek, E. Beucler, M. Drilleau, T. Kawamura, S. Kedar, N. Murdoch, P. Laudet (The InSight/SEIS Team), Science goals of SEIS, the InSight seismometer package, in *Lunar and Planetary Science Conference*. Lunar and Planetary Inst. Technical Report, vol. 46 (2015), p. 2272

- R.D. Lorenz, Y. Nakamura, J. Murphy, A bump in the night: wind statistics point to Viking 2 Sol 80 seismometer event as a real marsquake, in *47th Lunar and Planetary Science Conference* (2016), p. 1566
- D. Mimoun, P. Lognonne, W.B. Banerdt, K. Hurst, S. Deraucourt, J. Gagnepain-Beyneix, W.T. Pike, S.B. Calcutt, M. Bierwirth, R. Roll, P. Zweifel, D. Mance, O. Robert, T. Nebut, S. Tillier, P. Laudet, L. Kerjean, R. Perez, R. Giardini, U. Christensen, R. Garcia, The InSight SEIS experiment, in *Lunar and Planetary Science Conference*. Lunar and Planetary Inst. Technical Report, vol. 43 (2012), p. 1493
- D. Mimoun, N. Murdoch, P. Lognonne, K. Hurst, W.T. Pike, J. Hurley, T. Nebut, W.B. Banerdt (The SEIS Team), The noise model of the SEIS seismometer of the InSight mission to Mars. *Space Sci. Rev.* **211**(1–4), 383–428 (2017)
- N. Murdoch, D. Mimoun, R.F. Garcia, W. Rapin, T. Kawamuea, P. Lognonne, D. Banfield, W.B. Banerdt, Evaluating the wind-induced mechanical noise on the InSight seismometers. *Space Sci. Rev.* **211**(1–4), 429–455 (2017). <https://doi.org/10.1007/s11214-016-0311-y>
- W.T. Pike, I. Standley, Fabrication process and package design for use in a micromachined seismometer or other device. US 7,870,788, Jan 18, 2011
- W.T. Pike, I.M. Standley, W.J. Karl, S. Kumar, T. Semple, S.J. Vijendran, T. Hopf, Design, fabrication and testing of a micromachined seismometer with nano-g resolution, in *Proc. Transducers 2009*, Denver, June 21–25 (2009). Paper M4F.003
- W.T. Pike, I.M. Standley, S. Calcutt, A silicon microseismometer for Mars, in *Proc. 17th Transducers Conf.*, Barcelona, Spain, June 16–20 (2013). Paper M4A.006
- G.P. Roberts, B. Matthews, C. Bristow, L. Guerrieri, J. Vetterlein, Possible evidence of paleomarsquakes from fallen boulder populations, Cerberus Fossae, Mars. *J. Geophys. Res., Planets* **117**(E2), E02009 (2012). <https://doi.org/10.1029/2011JE003816>
- C. Rodgers, *Inverse Methods for Atmospheric Sounding: Theory and Practice* (World Scientific, Singapore, 2000)
- J. Taylor, Seismic exploration of Mars and the NASA InSight mission. PhD thesis, University of Bristol (2014)
- N.A. Teanby, Predicted detection rates of regional-scale meteorite impacts on Mars with the InSight short-period seismometer. *Icarus* **256**, 49–62 (2015)
- N.A. Teanby, J. Wookey, Seismic detection of meteorite impacts on Mars. *Phys. Earth Planet. Inter.* **186**, 70–80 (2011)
- N.A. Teanby, J. Stevanović, J. Wookey, N. Murdoch, J. Hurley, R. Myhill, N.E. Bowles, S.B. Calcutt, W.T. Pike, Seismic coupling of short-period wind noise through Mars' regolith for NASA's InSight Lander. *Space Sci. Rev.* **211**(1–4), 485–500 (2017)